Full paper

Constructing stress-release layer on Fe_7Se_8-based composite for highly stable sodium-storage

Song Chen [a,b], Shaozhuan Huang [b], Yuan-Fang Zhang [b,c], Shuang Fan [a,b], Dong Yan [a,b], Yang Shang [b], Mei Er Pam [b], Qi Ge [b,c], Yumeng Shi [a,d,**], Hui Ying Yang [b,c,*]

[a] International Collaborative Laboratory of 2D Materials for Optoelectronics Science and Technology of Ministry of Education, College of Optoelectronic Engineering, Shenzhen University, Shenzhen, 518060, China
[b] Pillar of Engineering Product Development, Singapore University of Technology and Design, 8 Somapah Road, 487372, Singapore
[c] Digital Manufacturing and Design Centre, Singapore University of Technology and Design, Singapore, 487372, Singapore
[d] Engineering Technology Research Center for 2D Material Information Function Devices and Systems of Guangdong Province, College of Optoelectronic Engineering, Shenzhen University, Shenzhen, 518060, China

ABSTRACT

Engineering multicomponent composite materials into tailored structure is of vital importance for developing advanced sodium ion batteries (SIBs). However, the mechanical stress intensification originating from severe volume expansion upon sodiation induces anisotropic swelling and anomalous structural changes, thus leading to electrode instability and inferior sodium storage performance. Herein, we propose a novel stress-release strategy by inserting of $MoSe_2$ nanosheets onto the surface of yolk-shell Fe_7Se_8@C composite to accommodate the volume expansion and stabilize the electrode. Bestowed by the unique superiority, the Fe_7Se_8@C@MoSe_2 composite manifests impressive sodium-storage performance in terms of high specific capacity (473.3 mAh g^{-1} at 0.1 A g^{-1}), excellent rate capability (274.5 mAh g^{-1} at 5.0 A g^{-1}) and long-term cycling stability (87.1% capacity retention after 600 cycles at 1.0 A g^{-1}). Finite element (FE) simulations confirm that the exterior $MoSe_2$ layer could significantly dissipate the stress caused by the sodiation-induced expansion of Fe_7Se_8 in the carbon layer. The primary sodium storage mechanisms and structural evolution are further revealed in details by *in situ* and *ex situ* investigations. More encouragingly, a practical sodium-ion full cell based on Fe_7Se_8@C@MoSe_2 anode is demonstrated with remarkable performances. This work strengthens the fundamental understanding of mechanical effect for sodium-storage behaviors and sheds light onto designing smart multi-compositional hybrids toward advanced energy storage devices.

1. Introduction

Transition metal compounds have aroused great interests as emerging candidates for sodium ion batteries (SIBs) because of their unique crystal structures and tunable stoichiometric compositions [1–4]. However, transition-metal oxides (MO) and transition-metal sulfides (MS) usually suffer from poor ion transport and the shuttle effect of soluble intermediated products such as polysulfide anions (S_x^{n-}), thus leading to inferior performance [5–7]. Recent works have demonstrated that metal selenides (MSe) show their exceptional physical and chemical properties distinguishing from their MO/MS counterparts [8].

In addition, the discharge product Na_2Se possesses higher electronic conductivity than those of transition metal oxides/sulfides (Na_2O/Na_2S). Moreover, the weaker bond of M-Se is expected to be kinetically favorable for conversion reactions [9–11].

Among various MSe, iron selenides with natural abundance and environmental benignity accomplish the major criteria for the commercial applications [12–16]. However, their sluggish sodium storage kinetics and unyielding volume changes during repeated cycles have induced inferior cycling stability and rate capability [17]. Theoretical calculation indicates that stress could be mitigated by engineering the electrode material to nanoscale or porous structures [18]. As a typical

example, prominent progresses in cycling lifespan and rate capability have been achieved via the scrupulous yolk-shell structure design. For example, Zhong et al. [19] have reported the yolk-shell iron selenide@carbon nanobox for lithium ion battery anode, which delivered a reversible capacity of 871.6 mAh g^{-1} after 250 cycles. Yoo et al. [20] have developed the yolk-shell structured iron selenide@iron oxide/-graphitic carbon microspheres for lithium ion battery anode, realizing enhanced lithium-storage capacity and cycling stability. Notwithstanding these successes, the application of SIBs in the aforementioned reports has been still restricted by the low tap density of the respective architecture owing to the existence of large void or gap spaces and other morphologic issues. More importantly, constructing huge void space may induce complete destruction of outer shells under tight calendering process. Therefore, it is meaningful to realize smart hybridization of iron selenide into tailored nanostructure with low void space and robust structure.

Recently, constructing hierarchical structures with another active buffer through nanocomposites has been proposed to effectively tackle the aforementioned issues. On one hand, the protected layer can further accommodate structural deformation; on the other hand, the formed heterointerface could greatly boost Na$^+$ capture/storage and then facilitate the Na$^+$ diffusion. Among various candidates, MoSe$_2$ has drawn significant attention due to its 2D graphene-like layered structure with large interlayer spacing and high mechanical strength [21–23]. More encouragingly, our previous work has proven that the hetero-interface between MoS$_2$ and Fe$_{1-x}$S could significantly reduce the sodium ion diffusion barrier and accelerate the charge transfer kinetics [24], which inspire us to design rational heterointerface based on selenides for enhanced sodium storage. However, the researchers either constructed coating layer or engineered heterostructure to achieve desirable cycling performance and rate capability. There are few reports about the coexistence of both buffer layer and heterointerface on iron selenide-based anode. Herein, we design a rational nanocomposite consisting of MoSe$_2$ layer coated on the yolk shell Fe$_7$Se$_8$@C structure to simultaneously realize the construction of both dual buffer layers and heterointerface. Benefiting from these smart configuration, Fe$_7$Se$_8$@C@MoSe$_2$ composite exhibits superior long-term cycling stability (87.1% capacity retention after 600 cycles at 1.0 A g^{-1}) and rate capability (274.5 mAh g^{-1} at 5.0 A g^{-1}). Finite element (FE) analyses combined with experimental results indicate that MoSe$_2$ nanosheet arrays onto the surface of yolk-shell Fe$_7$Se$_8$@C nanocubes could further suppress the sodiation-induced fracture in the carbon shell layer from a mechanical standpoint. Then the reaction mechanism and structural evolution have been thoroughly explored by *in situ* and *ex situ*
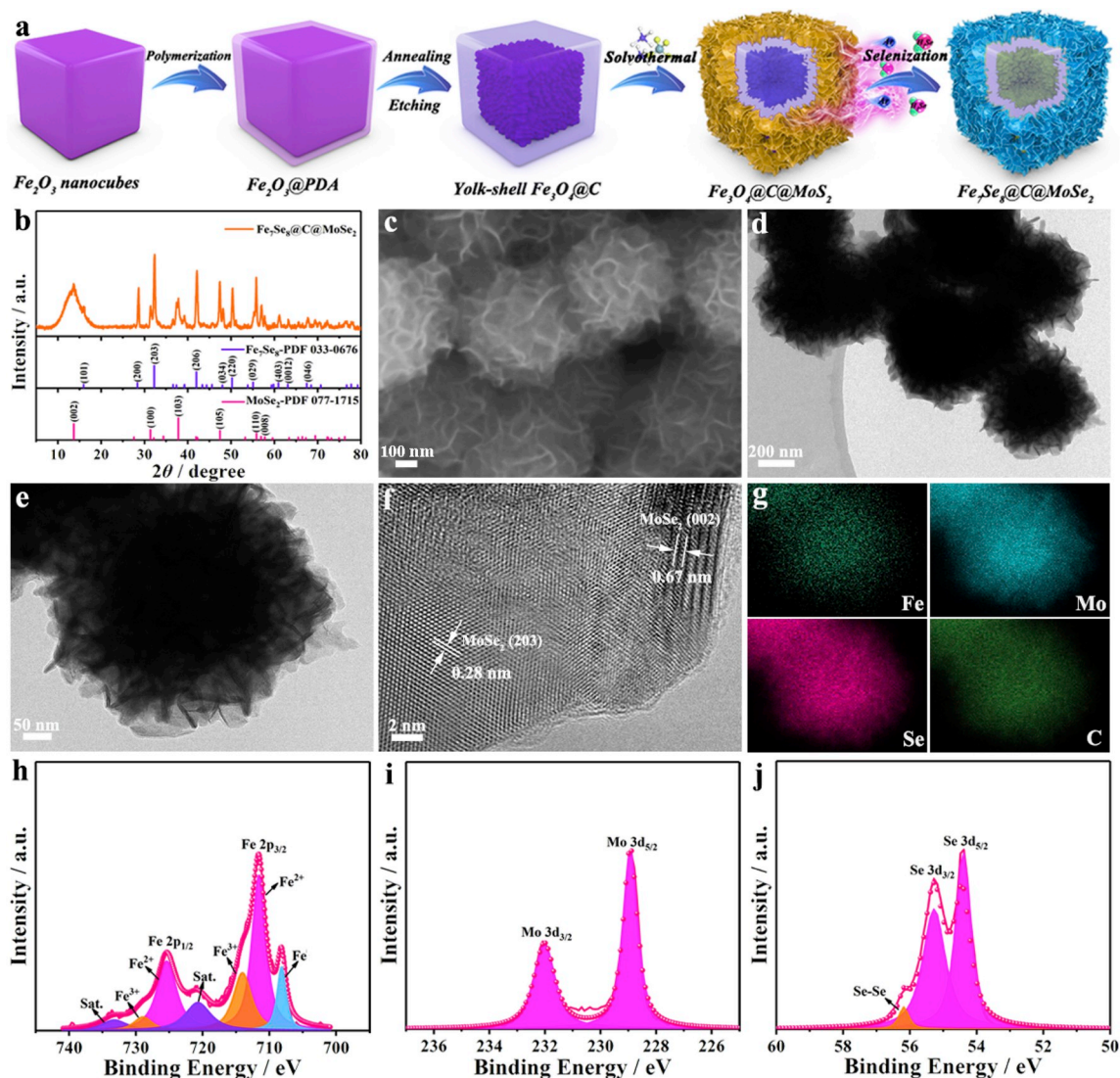

Fig. 1. (a) Schematic illustration of the synthesis process for Fe$_7$Se8@C@MoSe2 composite. (b) XRD pattern, (c) SEM, (d, e) TEM, (f) HRTEM images, (g) element mappings, and high-resolution XPS spectra of (h) Fe 2p, (i) Mo 3d and (j) Se 2p of Fe$_7$Se$_8$@C@MoSe$_2$ composite.

measurements. Furthermore, the full cell investigation further demonstrates that this unique composite electrode has great potential value for the next generation SIBs. The proposed strategy not only greatly improves the electrochemical performances of iron selenide-based anode, but also paves the way for engineering advanced multicomponent composites for high-performance energy storage devices.

2. Results and discussion

The synthesis processes of the Fe$_7$Se8@C@MoSe2 composite is illustrated in Fig. 1a. Firstly, uniform Fe$_2$O$_3$ nanocubes with an average size of 400 nm were synthesized via a facile coprecipitation method (Figs. S1a and 1b). Next, a uniform and smooth polydopamine (PDA) layer was polymerized on the surface of nanocubes (Fig. S1c). After annealing in Ar and subsequent etching by HCl, yolk-shell Fe$_3$O$_4$@C was obtained (Figs. S1d–f). Next, MoS$_2$ nanosheets were then uniformly grown on the surface of yolk-shell Fe$_3$O$_4$@C, forming an enlarged nanocube with size about 450 nm (Fig. S2). Finally, Fe$_7$Se8@C@MoSe2 composite was obtained without obvious structural change through a selenization treatment in Ar/H$_2$ atmosphere (Fig. 1b and c). The X-ray diffraction (XRD) pattern of the as-synthesized Fe$_7$Se8@C@MoSe2 composite can be well indexed to the mixed crystal structures of hexagonal Fe$_7$Se8 (JCPDS NO. 33–0676) and MoSe2 phases (JCPDS NO. 77–1715). Transmission electron microscopy (TEM) image confirms that MoSe$_2$ layer with a thickness of about 50 nm is strongly anchored on Fe$_3$O$_4$@C without visible interlayer gap between carbon and MoSe$_2$ layers (Fig. 1d and e). High-resolution TEM (HRTEM) image in Fig. 1f clearly displays the lattice fringes with *d*-spacing of 0.28 and 0.67 nm, corresponding to the (203) and (002) planes of MoSe$_2$, respectively [25]. No obvious lattice fringes belonging to Fe$_7$Se8 are observed owing to the coverage of MoSe$_2$ layer. Energy dispersive X-ray spectroscopy (EDS) elemental mapping images show the distribution of Fe, Mo, Se, and C elements, verifying the successful formation of Fe$_7$Se8@C@MoSe2 composite (Fig. 1g). For comparison, yolk-shell Fe$_7$Se8@C was also prepared by the same procedure without MoSe2. All the diffraction peaks can be indexed to the hexagonal Fe$_7$Se8 (JCPDS NO. 33–0676) without any impurities (Fig. S3a). SEM and TEM images indicate that the yolk-shell morphology is well maintained after a selenization process (Figs. S3b and c). The thickness of the carbon layer is about 20 nm. HRTEM image shows lattice fringes with *d*-spacing of 0.27 nm, corresponding to the (203) plane of Fe$_7$Se8 phase (Fig. S3d).

The X-ray photoelectron spectroscopy (XPS) survey scan further confirms the presence of Fe, Mo, Se, and C elements in the composite (Fig. S4). In the Fe 2p XPS spectrum (Fig. 1h), the peaks at 711.6 and 725.4 eV are related to Fe^{2+} in Fe$_7$Se8 along with a corresponding satellite at 720.7 and 733.2 eV, while the peaks located at 713.9 and 728.8 eV are attributed to Fe^{3+} originating from the partial surface oxidation [26,27]. In addition, the peak at 708.2 eV indicates the existence of the metallic Fe, which may be generated by the minor reduction of iron selenides [28,29]. Two sharp peaks observed at 228.9 and 231.1 eV in the Mo 3d XPS spectrum (Fig. 1i) are corresponded to Mo 3d$_{5/2}$ and Mo 3d$_{3/2}$, respectively [30,31]. The Se 3d XPS spectrum (Fig. 1j) shows two peaks at 54.4 and 55.3 eV associated with Se 3d$_{5/2}$ and Se 3d$_{3/2}$, respectively, whereas the peak at 56.2 eV is attributed to Se–Se bond from the incomplete reaction during the selenization process [27,32]. Based on the thermogravimetric analysis (TGA) result shown in Fig. S5, the weight percentage of Fe$_7$Se8, MoSe2 and carbon in the composite can be estimated to be 76.7%, 19.3% and 4.0%, respectively (see the detailed calculation process in Supporting Information). In addition, the nitrogen adsorption-desorption isotherms in Fig. S6 indicate that Fe$_7$Se8@C@MoSe2 composite possesses a higher Brunauer-Emmett-Teller (BET) surface area of 73.6 m^2 g^{-1} than those of Fe$_7$Se8@C (41.3 m^2 g^{-1}) and pure Fe$_7$Se8 (13.1 m^2 g^{-1}). The composite structures with high porosity could provide abundant contact area and diffusion channels for electrolyte.

Fig. 2 shows the sodium storage performance of Fe$_7$Se8@C@MoSe2,

Fe$_7$Se8@C and bare Fe$_7$Se8 electrodes. Cyclic voltammetry (CV) measurement was first carried out at a scan rate of 0.1 mV s^{-1}. As for Fe$_7$Se8@C@MoSe2 composite in the discharge process (Fig. 2a), there are four main peaks at about 1.71, 0.80, 0.53 and 0.25 V, corresponding to the multistep sodiation processes accompanied by the formation of solid electrolyte interphase (SEI) films [33–35]. For the anodic scan, two oxidation peaks at around 1.55 and 1.73 V are observed, implying the stepwise desodiation processes. The detailed reaction processes will be discussed in the subsequent *in situ* XRD section. From the second cycle onward, the CV curves basically overlap, suggesting good electrochemical reversibility and structural stability. Compared with Fe$_7$Se8@C@MoSe2, the Fe$_7$Se8@C and bare Fe$_7$Se8 electrodes both exhibit inferior reversibility, implying the poor electrochemical stability (Fig. S7).

Fig. 2b shows the galvanostatic charge-discharge profiles of Fe$_7$Se8@C@MoSe2 electrode after different cycles at 100 mA g^{-1}. This composite electrode delivers an initial discharge/charge capacity of 761.2/473.3 mAh g^{-1}, corresponding to an initial coulombic efficiency of 62.2%. The irreversible capacity loss is mainly attributed to the formation of SEI layer [36,37]. However, the Fe7Se8@C and bare Fe7Se8 electrodes deliver the lower initial coulombic efficiency of 60% and 58%, respectively, at the same current density. After 100 cycles, the Fe$_7$Se8@C@MoSe2 electrode remains a high reversible capacity of 423.7 mA h g^{-1}, displaying a higher capacity retention (89.5%) than Fe$_7$Se8@C (82.0%) and bare Fe$_7$Se8 (66.5%) electrodes (Fig. 2c). The higher specific capacity and better cyclability indicate the higher sodium-storage capability and better structural stability of Fe$_7$Se8@C@MoSe2 electrode. The fast capacity drops of Fe$_7$Se8@C and bare Fe$_7$Se8 indicates their structural instability during cycling, suggesting MoSe$_2$ nanosheet arrays assembled on the yolk-shell Fe$_7$Se8@C structure can effectively accommodate structural deformation during repeated cycles. *Ex-situ* SEM image after cycling strongly supports that the Fe$_7$Se8@C@MoSe2 almost maintains the structural integrity without obvious damage (Fig. S8).

Another attractive superiority is its outstanding rate capability (Fig. 2d). Notably, Fe$_7$Se8@C@MoSe2 demonstrates the best rate capability among the three electrodes: 750.2, 431.0, 407.9, 367.5, 331.1, 303.3 and 274.5 mAh g^{-1} at the current densities of 0.1, 0.2, 0.5, 1.0, 2.0, 3.0 and 5.0 A g^{-1}, respectively. In addition, the increase of current density only causes a very small change of overpotential (Fig. 2e), indicating the great sodium diffusion kinetics of Fe$_7$Se8@C@MoSe2. As revealed in our previous work [24], the improvement of Na$^+$ storage kinetics may be attributed to the formed heterointerface between MoSe$_2$ and carbon to reduce the sodium ion diffusion barrier. Remarkably, the rate performance is also better than most of other iron selenide-based nanostructures [14,16,38–43] (Fig. 2f), further verifying the prominent rate performance of this unique composite structure. Even after long-term cycling at 1.0 A g^{-1}, the reversible capacity basically maintains unchanged at about 345 mAh g^{-1} with 87.1% capacity retention up to 600 cycles, suggesting its superior high-rate cycling stability (Fig. 2g). Such exceptional rate capability could be mainly ascribed to the cooperative actions of stress-release layer and heterointerface to alleviate structural stress and to accelerate charge transfer.

To fundamentally explore the advantage of this structure design, we performed finite element (FE) analyses to further support our assumption that the MoSe$_2$ nanosheet arrays on the surface of yolk-shell Fe$_7$Se8@C nanocubes could further help reduce the risk of fracture in the carbon shell layer from a mechanical standpoint. The Fe$_7$Se8 yolk is similar to a cube with an edge length of 300 nm. The carbon shell has a thickness of 15 nm and creates an interior void space. The MoSe$_2$ nanosheets with a high of 50 nm are vertically attached onto the surface of the carbon shell. Fig. 3a shows the modeled undeformed geometry of one-eight of a Fe$_7$Se8@C nanocube by taking into account the symmetries. We assume a constant and uniform expansion coefficient throughout the yolk structure. The Young's modulus and Poisson's ratio of Fe$_7$Se8 are respectively 73 GPa and 0.179 [44,45]; those of the
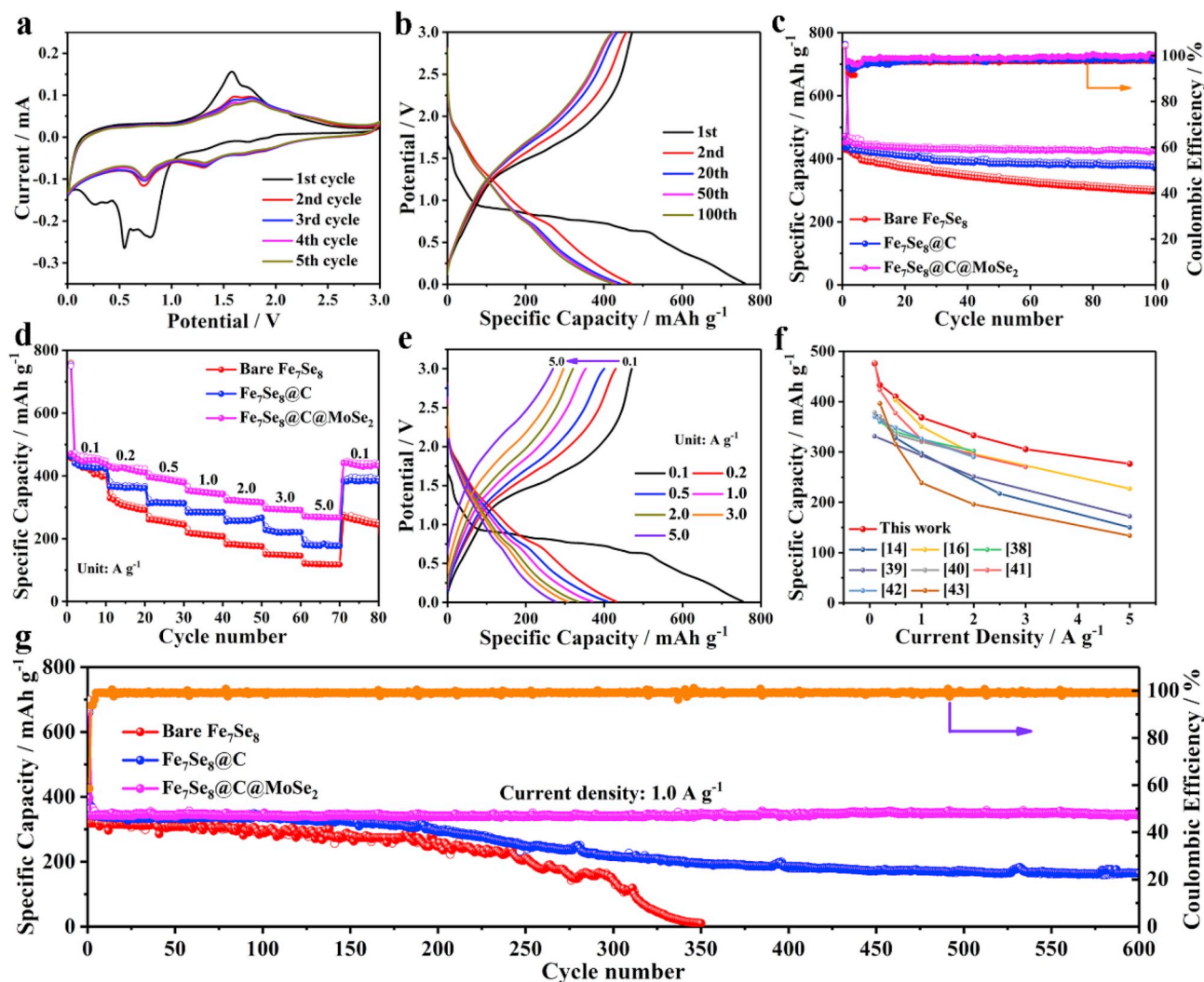
Fig. 2. (a) CV curves of Fe7Se8@C@MoSe2 composite electrode for the first five cycles. (b) Galvanostatic charge-discharge profiles of Fe7Se8@C@MoSe2 composite electrode at 100 mA g^{-1}. (c) Cycling performance at 100 mA g^{-1}. (d) Rate capability at various current densities. (e) Galvanostatic charge-discharge profiles of Fe7Se8@C@MoSe2 composite electrode at various current densities. (f) The comparison of the rate capability with other iron selenide-based anode materials previously reported [14,16,38–43]. (g) Long-term cycling performance at 1.0 A g^{-1}.
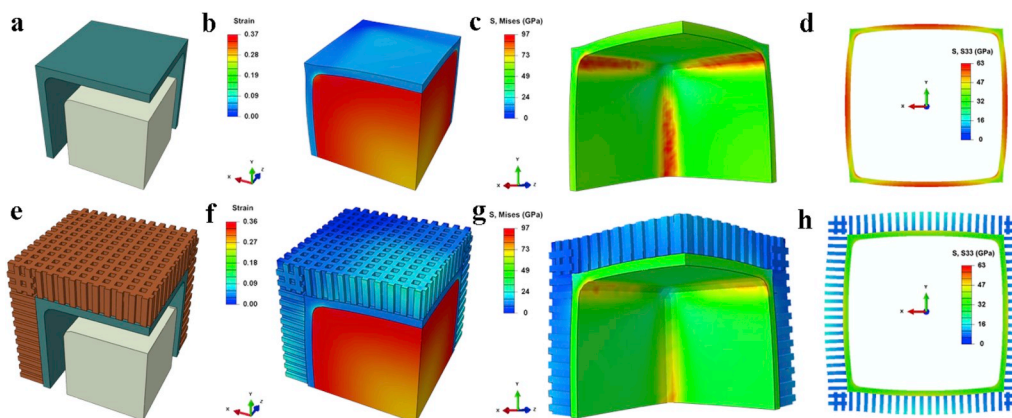

Fig. 3. FE simulations comparing the strain and stress distributions of (a–d) Fe7Se8@C and (e–h) Fe7Se8@C@MoSe2 structures after sodiation.

amorphous carbon shell are respectively 950 GPa and 0.2 [46]; and those of MoSe$_2$, 177 GPa and 0.23 [47]. The structures were discretized using tetrahedral elements (C3D4). During sodiation, the yolk structure first expands freely within the void space, then comes into contact with

the carbon shell (Fig. 3b) and induces severe stress concentration along the edges of the cubic carbon shell (Fig. 3c). The highest strain of 37% in Fig. 3b corresponds to a critical state where the in-plane tensile stress in the middle cross-section of the brittle carbon shell reaches its tensile

strength of 63 GPa and causes fracture (Fig. 3d). For a Fe_7Se_8@C@-$MoSe_2$ structure (Fig. 3e), a similar volume expansion level (Fig. 3f) results in a more uniform stress distribution in the shell structure (Fig. 3g). The in-plane tensile stress in the carbon shell is lower than 40 GPa (Fig. 3h). Therefore, the Fe_7Se_8@C@$MoSe_2$ structure can effectively mitigate the sodiation-induced fracture of the nanocubes, which ultimately results in exceptional electrochemical and structural stability shown in Fig. 2.

Galvanostatic intermittent titration technique (GITT) curves reveal that the multistep sodiation and desodiation reactions have a decisive impact on Na^+ diffusion coefficient (D_{Na}) (Fig. 4a and b and Fig. S9). Note that the diffusion coefficient of Fe_7Se_8@C@$MoSe_2$ electrode is minor fluctuant and higher than that of bare Fe_7Se_8 and Fe_7Se_8@C as a whole, which could be attributed to abundant phase boundaries forming crystal defects and active sites to facilitate ion diffusion [48]. Moreover, out-of-sync reactions of these two selenides can effectively relieve the structural stress during the sodiation/desodiation process, which is also beneficial to the diffusion of Na^+ [49].

Attracted by the exceptional rate performance, scan-rate-dependent CV measurements were investigated sequentially to interpret the detailed kinetic behaviors (Fig. 4c and Fig. S10). The relationship between the peak current (i) and scan rate (v) obeys the power law equation: $i = av^b$, where both a and b are constants [50–52]. The b-value of 0.5 represents a diffusion-controlled behavior, whereas 1.0 corresponds to a surface capacitive process. As shown in Fig. 4d, the b values obtained from the log (v) *versus* log (i) plots for peak 1, 2 and 3 are 0.92, 0.94, and 0.91, respectively, suggesting a pseudocapacitive-controlled sodiation mechanism in Fe_7Se_8@C@$MoSe_2$ composite. Generally, the total capacitance could be divided into two aspects: surface pseudocapacitive contribution (k_1v) and diffusion-controlled contribution ($k_2v^{1/2}$) at a given scan rate [53]. More specifically, the capacitive

contributions are evaluated to be about 40.3, 55.0 and 78.4% at 1.0 mV s^{-1} (Fig. 4e and Fig. S10). With the increase of scan rates, the fraction of diffusion-controlled contribution is decreasing, and the pseudocapacitance contribution enlarges (Fig. 4f). The highest surface capacitive contribution unambiguously illustrates the fundamental origin about the best rate capability of Fe_7Se_8@C@$MoSe_2$ among these three samples [50].

In situ electrochemical impedance spectroscopy (EIS) during the first sodiation/desodiation process was performed to explore kinetics differences caused by phase evolution at different discharge/charge states (Fig. 4g and Fig. S11). Although these three electrodes show the similar variation tendency on the whole, Fe_7Se_8@C@$MoSe_2$ presents the smallest charge-transfer resistances. EIS spectra after different cycles demonstrate the low and steady resistance values of Fe_7Se_8@C@$MoSe_2$ electrode from the 20th cycle onward (Fig. 4h and Fig. S12), suggesting the stable charge transfer behaviors on the electrode/electrolyte interface [54–56]. Especially, Fe_7Se_8@C@$MoSe_2$ manifests the highest D_{Na} throughout the entire cycles, confirming the advantages of carbon and $MoSe_2$ encapsulation in enhancing charge transfer properties (Fig. 4i).

To further reveal the reaction mechanism and structural evolution of Fe_7Se_8@C@$MoSe_2$, *in situ* XRD was conducted during the first and second sodiation/desodiation processes (Fig. 5a and b). Noted that the strong peaks located at around 27.5°, 43.8° and 46.0° are indexed to carbon paper, BeO and Be, respectively. In the XRD contour map, the peaks at 28.8°, 32.5° and 42.1° correspond to the (200), (203) and (206) planes of Fe_7Se_8, and the peaks at 13.6°, 31.4°, 37.8° and 47.5° are ascribed to (002), (100), (103) and (105) planes of $MoSe_2$. As the sodiation proceeds (stage I), these peaks gradually shift to lower 2θ, implying the lattice expansion induced by Na^+ insertion to Fe_7Se_8 and $MoSe_2$. When continuously discharging to 0.01 V (stage II), these peaks gradually disappear; meanwhile the diffraction peak at about 37.5°
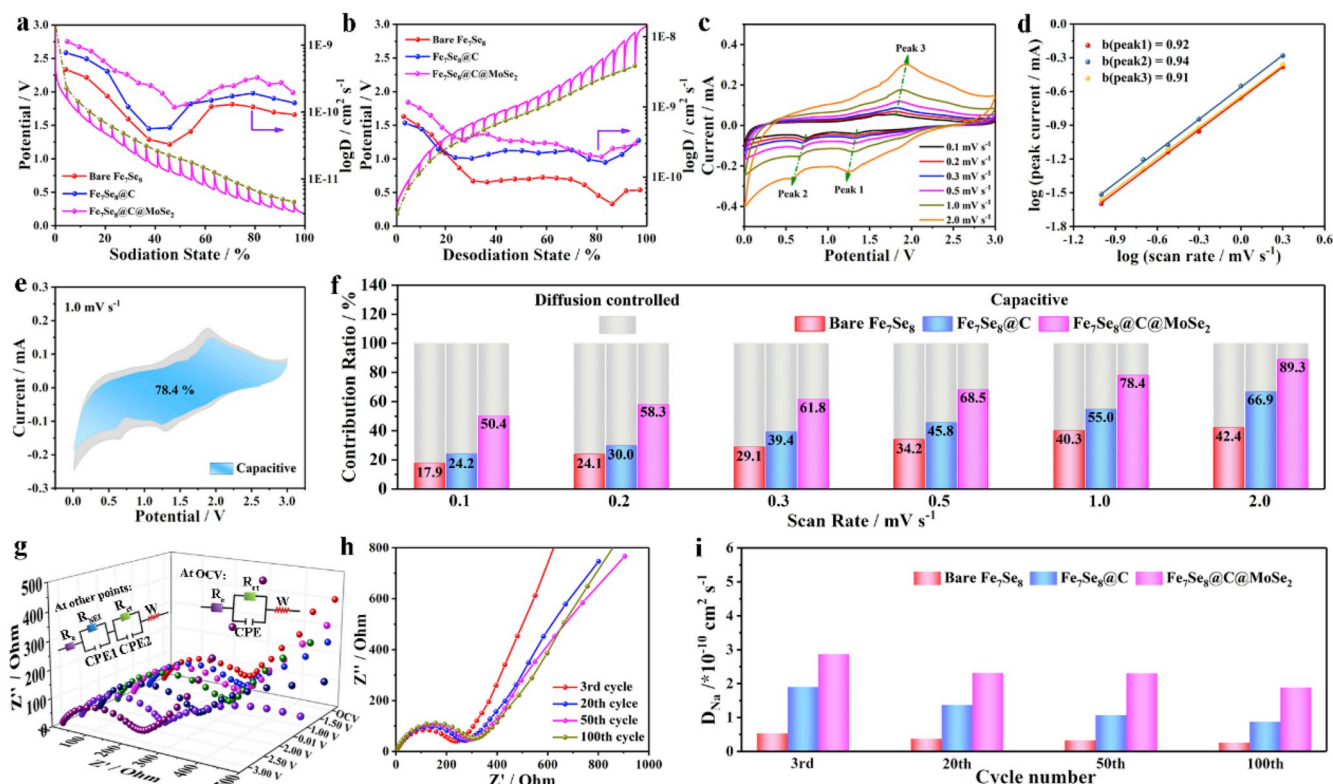

Fig. 4. GITT curves and the corresponding Na^+ diffusion coefficient at (a) the discharge process and (b) the charge process of three electrodes. (c) CV curves of Fe_7Se_8@C@$MoSe_2$ composite at different scan rates. (d) Linear relationship between log (i) and log (v). (e) Capacitive and diffusion-controlled contribution of Fe_7Se_8@C@$MoSe_2$ at 1.0 mV s^{-1}. (f) Normalized contribution ratio of capacitive capacities of three samples at different scan rates. (g) *In situ* EIS spectra evolution at different charge/discharge potentials and (h) the Nyquist plots at different cycles of Fe_7Se_8@C@$MoSe_2$. (i) Variation chart of Na^+ diffusion coefficient (D_{Na}) for these three electrodes.
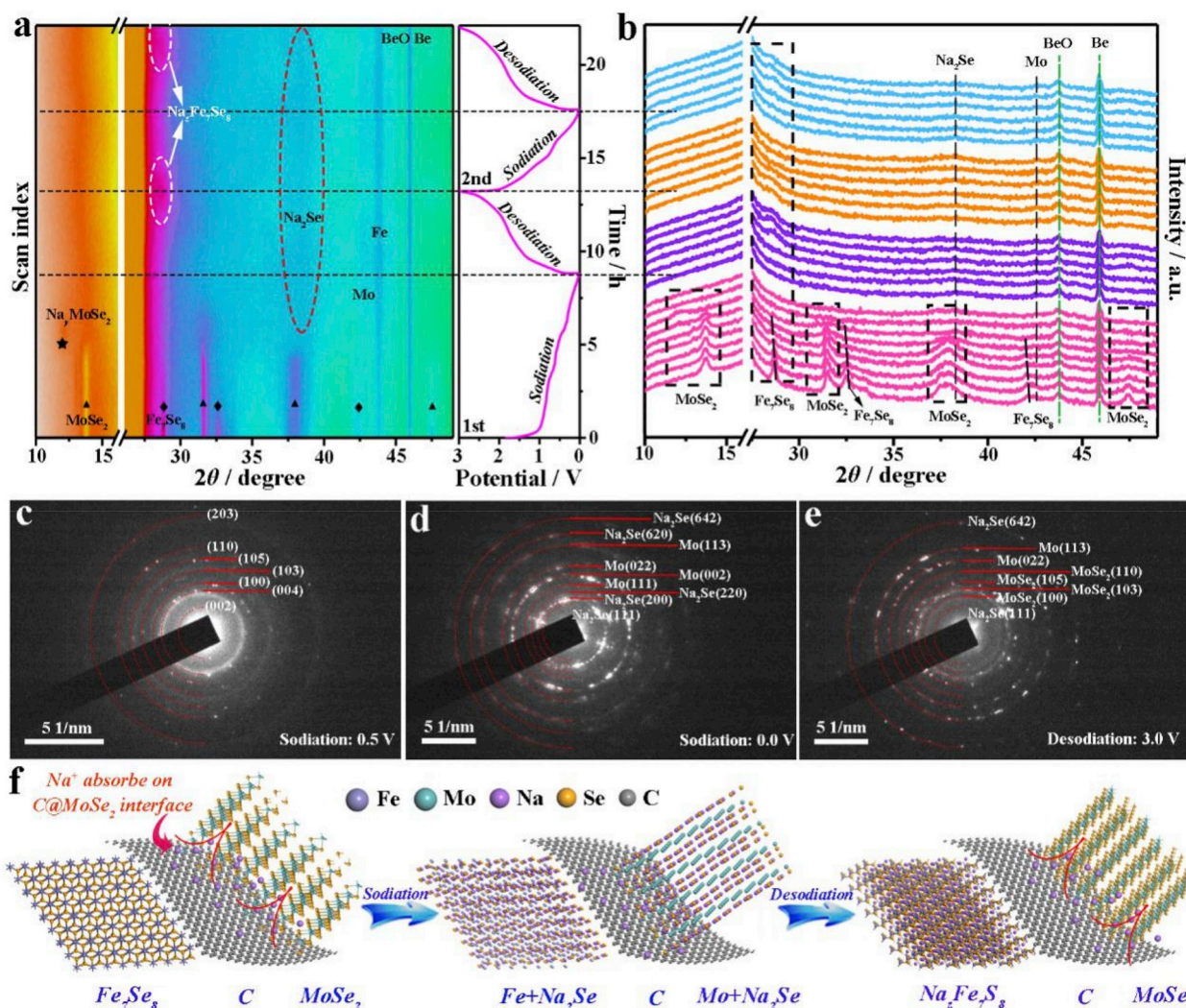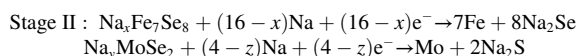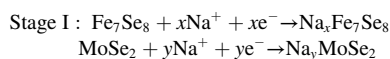
Fig. 5. (a) Contour plots of *in situ* XRD results and (b) selected diffraction patterns during the first and second sodiation/desodiation processes. (c–e) Ex situ SAED patterns at different states of sodiation/desodiation. (f) Proposed schematic atomistic models of the illustrated reaction mechanism for Fe7Se8@C@MoSe2 composite during the sodiation and desodiation process.
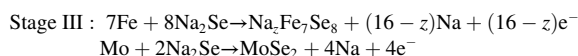
corresponding to Na2Se (JCPDS No. 96-101-1379) emerges and becomes stronger and stronger. The formation of Na2Se signifies the conversion reactions between $Na_xFe_7Se_8$/Na_yMoSe_2 and Na^+ accompanied by the formation of metallic Fe^0 ($\approx 44.0°$, JCPDS No. 96-110-0109) and Mo^0 ($\approx 43.4°$, JCPDS No. 96-900-8475). In subsequent desodiation process (stage III), the diffraction peak corresponding to Na2Se gradually disappears, indicating the reversible conversion between Na2Se and Fe^0/Mo^0. However, the peak at about 27.5° does not turn back its initial position at fully charged state, implying the reaction cannot return to Fe7Se8 phase. The peak of intermediate product $Na_zFe_7Se_8$ at about 28.2° is also observed in the first and second desodiation processes. Nevertheless, the MoSe2 peaks could not be detected at the end of charge process, suggesting the poor crystallinity nature of the product upon deintercalation [57,58]. The *ex situ* SAED patterns of Fe7Se8@C@MoSe2 at different sodiation/desodiation states were further analyzed (Fig. 5c–e). When discharged to 0.5 V (Fig. 5c), the SAED pattern shows a series of weakened diffraction rings, corresponding to the sodiated MoSe2. At fully discharged state (Fig. 5d), the SAED pattern indicates that the Na_yMoSe2 is transformed into Na2Se and metallic Mo, validating the accomplishment of conversion reaction. After recharged back to 3.0 V (Fig. 5e), the diffraction rings of MoSe2 are detected, confirming the reversible conversion reaction. However, no obvious diffraction rings of Fe7Se8 and its products are observed due to the

coverage of dual-protected layers. The presence of metal Fe^0 at the end of sodiation process is further confirmed by the SAED pattern of bare Fe7Se8 in Fig. S13a. Meanwhile, several diffraction rings at fully charged 3.0 V close to the iron selenide, which should be indexed to $Na_zFe_7Se_8$ (Fig. S13b). Therefore, based on the aforementioned *in situ* XRD and *ex situ* SAED pattern analysis, the multistep reaction mechanisms for Fe7Se8@C@MoSe2 at different sodiation/desodiation states could be elucidated as follows:

Sodiation process:

$$Stage\ I:\ Fe_7Se_8 + xNa^+ + xe^- \rightarrow Na_xFe_7Se_8$$
$$MoSe_2 + yNa^+ + ye^- \rightarrow Na_yMoSe_2$$

$$Stage\ II:\ Na_xFe_7Se_8 + (16-x)Na + (16-x)e^- \rightarrow 7Fe + 8Na_2Se$$
$$Na_yMoSe_2 + (4-z)Na + (4-z)e^- \rightarrow Mo + 2Na_2S$$

Desodiation process:

$$Stage\ III:\ 7Fe + 8Na_2Se \rightarrow Na_zFe_7Se_8 + (16-z)Na + (16-z)e^-$$
$$Mo + 2Na_2Se \rightarrow MoSe_2 + 4Na + 4e^-$$

The corresponding schematic illustration of reaction mechanism was also proposed as depicted in Fig. 5f. The Fe7Se8@C@MoSe2 composite is composed of the hexagonal Fe7Se8, carbon layer and 2D layered MoSe2 nanosheets. Based on our previous work [24], the superficial

carbon and MoSe$_2$ layer with heterointerface could significantly reduce sodium ion diffusion barrier, thus forming the so-called "Na$^+$ reservoir" to accelerate the reaction kinetics. Upon discharging, the assembled MoSe$_2$ nanosheets could facilitate the electrolyte permeation. Thanks to the low diffusion barrier, a lot of sodium ions absorbe on the interface of C@MoSe$_2$. High concentration gradient actuates Na$^+$ to pump into the interior structure, thus achieving a superior reaction kinetics. After full sodiation state, Fe$_7$Se$_8$/MoSe2 are converted into Fe/Mo metals and Na$_2$Se. During the charge process, Mo nanoclusters could act as "pin conductor" until MoSe$_2$ phase is formed, meanwhile Fe and Na$_2$Se are transformed into Na$_z$Fe$_7$Se$_8$. Such a significant promotion could be maintained in the subsequent cycles owing to the heterointerfacial regeneration after desodiation. Therefore, from the above analysis, the exceptional sodium storage performance of Fe$_7$Se$_8$@C@MoSe2 composite could be mainly ascribed to its structural design: (1) MoSe$_2$ nanosheets anchored on carbon layer ensure good mechanical strength to buffer structural stress during cycling; (2) the heterointerface between carbon and MoSe$_2$ may be effectively lower Na-ions diffusion barrier and facilitate charge transfer kinetic [24]; (3) the void space between Fe$_7$Se$_8$ and carbon layer can afford a spatial confinement to mitigate the volume change; (4) the carbon layer decoration enhances the electrical conductivity and structural integrity.

To further investigate the commercial viability, a full cell comprising the Fe$_7$Se$_8$@C@MoSe2 composite anode and Na$_3$V$_2$(PO$_4$)$_3$/C cathode was assembled (Fig. 6a). The Na$_3$V$_2$(PO$_4$)$_3$/C electrode delivers a reversible specific capacity of ~85 mAh g^{-1} at 100 mA g^{-1} in half-cell (Fig. S14). The full cell was carried out within the voltage window of 1.0–3.5 V, and the specific capacity was evaluated based on the anode mass. As shown in Fig. 6b, the Fe$_7$Se8@C@MoSe2//Na$_3$V$_2$(PO$_4$)$_3$/C full cell exhibits the first discharge/charge capacity of 397.2/383.1 mAh g^{-1}, corresponding to the coulombic efficiency of 96.4%. In addition, the full cell shows the distinct discharge/charge voltage plateau at about 2.7/2.1 V, achieving a high energy conversion efficiency of 75.0%. Even after 100 cycles, it still delivers a reversible capacity of 376.8 mAh g^{-1} with capacity retention of 94.8%. More encouragingly, the full cell also exhibits an outstanding rate capability: reversible capacities of 392.7, 382.4, 373.6, 352.2 and 329.3 mA h g^{-1} at current densities of 0.1, 0.2, 0.3, 0.5 and 1.0 A g^{-1}, respectively. The superior electrochemical performance of the sodium-ion full cell demonstrates that the Fe$_7$Se8@C@MoSe2 shows competitive merits and great prospects for practical applications.

3. Conclusion

In summary, we have designed and fabricated a novel Fe$_7$Se$_8$-based anode with dual protected layers of carbon and MoSe$_2$ nanosheets to simultaneously realize the construction of buffer layer and heterointerface. FE simulations reveal that MoSe$_2$ layers could effectively accommodate sodiation-induced fracture in the carbon layer from a mechanical standpoint. Interesting merits including strong mechanical stability, fast charge transfer and high electronic conductivity are intimately merged in Fe$_7$Se8@C@MoSe2 composite structure. As a preliminary test, this composite delivers high sodium storage capacity (473.3 mAh g^{-1} at 0.1 A g^{-1}), exceptional rate capability (274.5 mAh g^{-1} at 5.0 A g^{-1}) and long-term cycling stability (87.1% capacity retention after 600 cycles at 1.0 A g^{-1}). *In situ* and *ex situ* technologies elucidate clearly the dominant mechanisms of sodiation kinetics, phase transformation and structural evolution process. Furthermore, coupled with a Na$_3$V$_2$(PO$_4$)$_3$@C, the sodium ion full cell still exhibits excellent cycling performance and rate capability as well as high energy conversion efficiency. Therefore, our findings demonstrate a new tactic of tailoring advanced multicomponent composites in the energy-storage field.
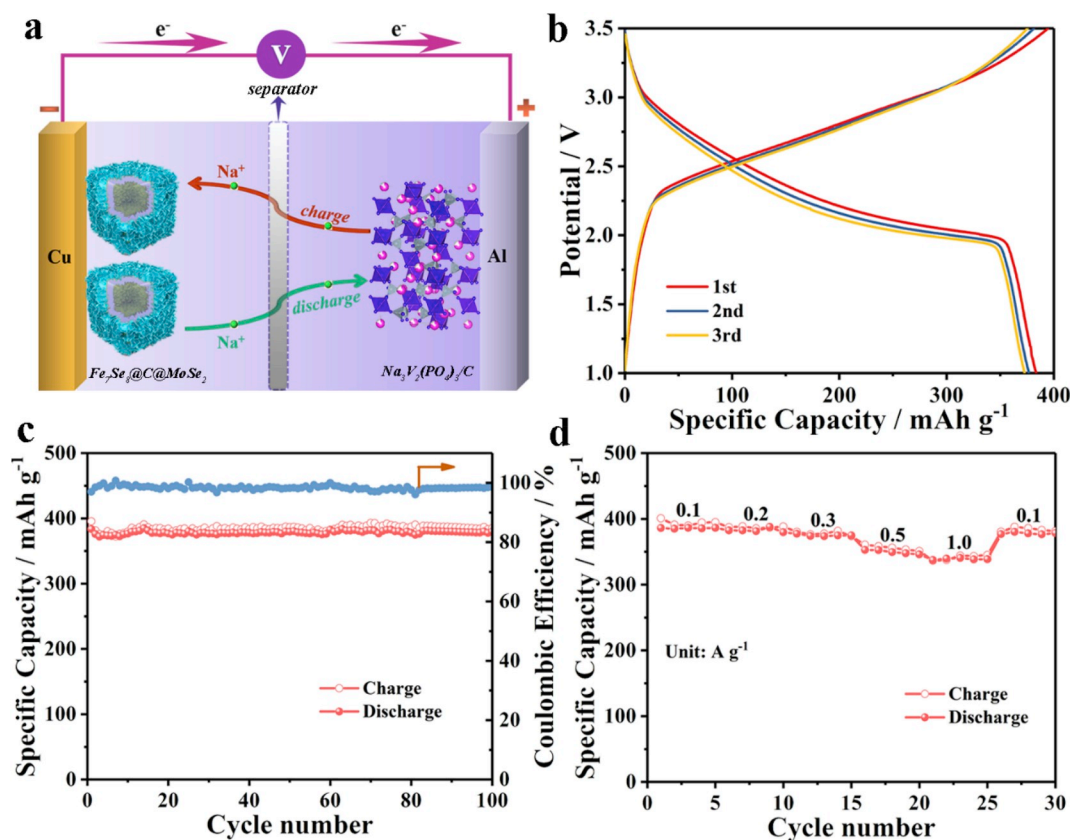

Fig. 6. Electrochemical characterization of the full cell (Fe$_7$Se8@C@MoSe2//Na$_3$V$_2$(PO$_4$)$_3$/C). (a) Schematic illustration for the structure of full cell. (b) Galvanostatic charge/discharge profiles. (c) Cycling performance at 0.1 A g^{-1}. (d) Rate performance of the full cell.

Declaration of competing interest

Appendix A. Supplementary data

Supplementary data to this article can be found online at https://doi. org/10.1016/j.nanoen.2019.104389.

References

[1] J.Y. Hwang, S.T. Myung, Y.K. Sun, Sodium-ion batteries: present and future, Chem. Soc. Rev. 46 (2017) 3529.

[2] Y. Shang, X. Li, S. Huang, S. Chen, Z. Yang, L. Guo, H.Y. Yang, A selective reduction approach to construct robust Cu$_{1.81}$S truss-structures for high-performance sodium storage, Matter (2020), https://doi.org/10.1016/j.matt.2019.10.027.

[3] J. Nan, X. Guo, J. Xiao, X. Li, W. Chen, W. Wu, H. Liu, Y. Wang, M. Wu, G. Wang, Nanoengineering of 2D MXene-based materials for energy storage applications, Small 15 (2019), 1902085.

[4] H. Liu, X. Liu, W. Li, X. Guo, Y. Wang, G. Wang, D. Zhao, Porous carbon composites for next generation rechargeable lithium batteries, Adv. Energy Mater. 7 (2017), 1700283.

[5] P. Ge, S. Li, L. Xu, K. Zou, X. Gao, X. Cao, G. Zou, H. Hou, X. Ji, Hierarchical hollow-microsphere metal-Selenide@Carbon composites with rational surface engineering for advanced sodium storage, Adv. Energy Mater. 9 (2019), 1803035.

[6] Y. Huang, Z. Wang, Y. Jiang, S. Li, Z. Li, H. Zhang, F. Wu, M. Xie, L. Li, R. Chen, Double-helix structure in carrageenan-metal hydrogels: a general approach to porous metal sulfides/carbon aerogels with excellent sodium-ion storage, Angew. Chem. Int. Ed. 55 (2016) 15925.

[7] C.P. Yang, S. Xin, Y.X. Yin, H. Ye, J. Zhang, Y.G. Guo, An advanced selenium-carbon cathode for rechargeable lithium-selenium batteries, Angew. Chem. Int. Ed. 52 (2013) 8363.

[8] Z. Hu, Q. Liu, S. Chou, S. Dou, Advances and challenges in metal sulfides/selenides for next-generation rechargeable sodium-ion batteries, Adv. Mater. 29 (2017), 1700606.

[9] P. Ge, C. Zhang, H. Hou, B. Wu, L. Zhou, S. Li, T. Wu, J. Hu, L. Mai, X. Ji, Anions induced evolution of Co$_3$X$_4$ (X = O, S, Se) as sodium-ion anodes: the influences of electronic structure, morphology, electrochemical property, Nano Energy 48 (2018) 617.

[10] X. Yang, J. Zhang, Z. Wang, H. Wang, C. Zhi, D.Y.W. Yu, A.L. Rogach, Carbon-supported nickel selenide hollow nanowires as advanced anode materials for sodium-ion batteries, Small 14 (2018), 1702669.

[11] P. Ge, H. Hou, C.E. Banks, C.W. Foster, S. Li, Y. Zhang, J. He, C. Zhang, X. Ji, Binding MoSe$_2$ with carbon constrained in carbonous nanosphere towards high-capacity and ultrafast Li/Na-ion storage, Energy Storage Mater 12 (2018) 310.

[12] F. Zhao, S. Shen, L. Cheng, L. Ma, J. Zhou, H. Ye, N. Han, T. Wu, Y. Li, J. Lu, Improved sodium-ion storage performance of ultrasmall iron selenide nanoparticles, Nano Lett. 17 (2017) 4137.

[13] Y. Huang, Z. Wang, Y. Jiang, S. Li, Z. Li, H. Zhang, F. Wu, M. Xie, L. Li, R. Chen, Hierarchical porous Co$_{0.85}$Se@reduced graphene oxide ultrathin nanosheets with vacancy-enhanced kinetics as superior anodes for sodium-ion batteries, Nano Energy 53 (2018) 524.

[14] X. Xu, J. Liu, J. Liu, L. Ouyang, R. Hu, H. Wang, L. Yang, M. Zhu, A general metal-organic framework (MOF)-Derived selenidation strategy for in situ carbon-encapsulated metal selenides as high-rate anodes for Na-ion batteries, Adv. Funct. Mater. 28 (2018), 1707573.

[15] K. Zhang, Z. Hu, X. Liu, Z. Tao, J. Chen, FeSe$_2$ microspheres as a high-performance anode material for Na-ion batteries, Adv. Mater. 27 (2015) 3305.

[16] P. Ge, H. Hou, S. Li, L. Yang, X. Ji, Tailoring rod-like FeSe$_2$ coated with nitrogen-doped carbon for high-performance sodium storage, Adv. Funct. Mater. 28 (2018), 1801765.

[17] H. Yin, Q. Li, M. Cao, W. Zhang, H. Zhao, C. Li, K. Huo, M. Zhu, Nanosized-bismuth-embedded 1D carbon nanofibers as high-performance anodes for lithium-ion and sodium-ion batteries, Nano Res 10 (2017) 2156.

[18] X.H. Liu, L. Zhong, S. Huang, S.X. Mao, T. Zhu, J.Y. Huang, Size-dependent fracture of silicon nanoparticles during lithiation, ACS Nano 6 (2012) 1522.

[19] D. Zhong, J. Chen, J. Zhang, Y. Luo, Z. Li, L. Cheng, Y. Chen, G. Wang, R. Wang, The yolk-shell FeSe@C nanobox with novel synthesis and its high performance for the anode of lithium-ion batteries, Mater. Res. Express 6 (2019), 085058.

[20] Y. Yoo, Y.J. Hong, Y.C. Kang, Rationally designed microspheres consisting of yolk-shell structured FeSe$_2$-Fe$_2$O$_3$ nanospheres covered with graphitic carbon for lithium-ion batteries, J. Mater. Chem. A 6 (2018) 15182–15190.

[21] D. Xie, X. Xia, Y. Zhong, Y. Wang, D. Wang, X. Wang, J. Tu, Exploring advanced sandwiched arrays by vertical graphene and N-doped carbon for enhanced sodium storage, Adv. Energy Mater. 7 (2017), 1601804.

[22] Y. Wang, Y. Wang, W. Kang, D. Cao, C. Li, D. Cao, Z. Kang, D. Sun, R. Wang, Y. Cao, TiO$_2$-Coated interlayer-expanded MoSe$_2$/phosphorus doped carbon nanospheres for ultrafast and ultralong cycling sodium storage, Adv. Sci. 6 (2019), 1801222.

[23] S. Zhang, G. Wang, J. Jin, L. Zhang, Z. Wen, J. Yang, Robust and conductive red MoSe$_2$ for stable and fast lithium storage, ACS Nano 12 (2018) 4010.

[24] S. Chen, S. Huang, J. Hu, S. Fan, Y. Shang, M.E. Pam, X. Li, Y. Wang, T. Xu, Y. Shi, H.Y. Yang, Boosting sodium storage of Fe$_{1-x}$S/MoS$_2$ composite via heterointerface engineering, Nano-Micro Lett. (2019), https://doi.org/10.1007/s40820-019-0311-z.

[25] L. Tang, B. Zhang, C. An, H. Li, B. Xiao, J. Li, Z. He, J. Zheng, Ultrahigh-rate behavior anode materials of MoSe$_2$ nanosheets anchored on dual-heteroatoms functionalized graphene for sodium-ion batteries, Inorg. Chem. 58 (2019) 8169.

[26] W. Chen, X. Zhang, L. Mi, C. Liu, J. Zhang, S. Cui, X. Feng, Y. Cao, C. Shen, High-performance flexible freestanding anode with hierarchical 3D carbon-networks/Fe$_7$S$_8$/graphene for applicable sodium-ion batteries, Adv. Mater. 31 (2019), 1806664.

[27] H. Yin, H. Qu, Z. Liu, R. Jiang, C. Li, M. Zhu, Long cycle life and high rate capability of three dimensional CoSe$_2$ grainattached carbon nanofibers for flexible sodium-ion batteries, Nano Energy 58 (2019) 715.

[28] Y. Xiao, J.Y. Hwang, I. Belharouak, Y.K. Sun, Na-storage capability investigation of carbon nanotubes-encapsulated Fe$_{1-x}$S composite, ACS Energy Lett 2 (2017) 364.

[29] K.J. Kim, D.W. Moon, K.L. Sun, K.H. Jung, formation of a highly oriented FeO thin film by phase transition of Fe$_3$O$_4$ and Fe nanocrystallines, Thin Solid Films 360 (2000) 118.

[30] H. Yin, Y. Jin, N. Yu, H. Qu, Z. Liu, R. Jiang, C. Li, M. Zhu, Graphene-like MoS$_2$ nanosheets on carbon fabrics as high performance binder-free electrodes for supercapacitors and Li-ion batteries, ACS Omega 3 (2018) 17466.

[31] J.S. Park, Y.C. Kang, Multicomponent (Mo, Ni) metal sulfide and selenide microspheres with empty nanovoids as anode materials for Na-ion batteries, J. Mater. Chem. A 5 (2017) 8616.

[32] J.H. Choi, S.K. Park, Y.C. Kang, A salt-templated strategy toward hollow iron selenides-graphitic carbon composite microspheres with interconnected multicavities as high-performance anode materials for sodium-ion batteries, Small 15 (2019), 1803043.

[33] S. Chen, Z. Chen, Y. Luo, M. Xia, C. Cao, Silicon hollow sphere anode with enhanced cycling stability by a template free method, Nanotechnology 28 (2017) 165404.

[34] Q. Wang, W. Zhang, C. Guo, Y. Liu, C. Wang, Z. Guo, In situ construction of 3D interconnected FeS@Fe$_3$C@graphitic carbon networks for high-performance sodium-ion batteries, Adv. Funct. Mater. 27 (2017), 1703390.

[35] S. Chen, Z. Chen, X. Xu, C. Cao, M. Xia, Y. Luo, Scalable 2D mesoporous silicon nanosheets for high-performance lithium-ion battery anode, Small 14 (2018), 1703361.

[36] H. Yin, X. Yu, Y. Yu, M. Cao, H. Zhao, C. Li, M. Zhu, Tellurium nanotubes grown on carbon fiber cloth as cathode for flexible all-solid-state lithium-tellurium batteries, Electrochim. Acta 282 (2018) 870.

[37] S. Chen, Y. Shi, Y. Wang, Y. Shang, W. Xia, H.Y. Yang, An all manganese-based oxide nanocrystal cathode and anode for high performance lithium-ion full cells, Nanoscale Adv 1 (2019) 1714.

[38] K. Wu, F. Chen, Z. Ma, B. Guo, Y. Lyu, P. Wang, H. Yang, Q. Li, H. Wang, A. Nie, In situ TEM and half-cell investigation of sodium storage in hexagonal FeSe nanoparticles, Chem. Commun. 55 (2019) 5611.

[39] M. Wan, R. Zeng, K. Chen, G. Liu, W. Chen, L. Wang, N. Zhang, L. Xue, W. Zhang, Y. Huang, Fe$_7$S$_8$ nanoparticles encapsulated by nitrogen-doped carbon with high sodium storage performance and evolving redox reactions, Energy Storage Mater 10 (2018) 114.

[40] Y. Long, J. Yang, X. Gao, X. Xu, W. Fan, J. Yang, S. Hou, Y. Qian, Solid-solution anion-enhanced electrochemical performances of metal sulfides/selenides for sodium-ion capacitors: the case of FeS$_{2-x}$Se$_x$, ACS Appl. Mater. Interfaces 10 (2018) 10945.

[41] G.D. Park, J.S. Cho, J.K. Lee, Y.C. Kang, Na-ion storage performances of FeSe$_x$ and Fe$_2$O$_3$ hollow nanoparticles-decorated reduced graphene oxide balls prepared by nanoscale Kirkendall diffusion process, Sci. Rep. 6 (2016) 22432.

[42] C. Lv, H. Liu, D. Li, S. Chen, H. Zhang, X. She, X. Guo, D. Yang, Ultrafine FeSe nanoparticles embedded into 3D carbon nanofiber aerogels with FeSe/Carbon interface for efficient and long-life sodium storage, Carbon 143 (2019) 106.

[43] F. Kong, L. Lv, Y. Gu, S. Tao, X. Jiang, B. Qian, L. Gao, Nano-sized FeSe$_2$ anchored on reduced graphene oxide as a promising anode material for lithium-ion and sodium-ion batteries, J. Mater. Sci. 54 (2019) 4225.

[44] S. Chandra, A.K.M.A. Islam, Elastic properties of mono-and poly-crystalline PbO-type FeSe$_{1-x}$Te$_x$ (x=0-1.0): a first-principles study, Phys. C Supercond. 470 (2010) 2072.

[45] A. Cavallin, V. Sevriuk, K. N. Fischer, S. Manna, S. Ouazi, M. Ellguth, C. Tusche, H. L. Meyerheim, D. Sander, J. Kirschner, Preparation and characterization of Bi_2Se_3 (0001) and of epitaxial FeSe nanocrystals on Bi_2Se_3 (0001), Surf. Sci. 646 (216) 72.

[46] M.F. Yu, O. Lourie, M.J. Dyer, K. Moloni, T.F. Kelly, R.S. Ruoff, Strength and breaking mechanism of multiwalled carbon nanotubes under tensile load, Science 287 (2000) 637.

[47] Y. Yang, X. Li, M. Wen, E. Hacopian, W. Chen, Y. Gong, J. Zhang, B. Li, W. Zhou, P. M. Ajayan, Q. Chen, T. Zhu, J. Lou, Brittle fracture of 2D $MoSe_2$, Adv. Mater. 29 (2017), 1604201.

[48] G. Fang, Z. Wu, J. Zhou, C. Zhu, X. Cao, T. Lin, Y. Chen, C. Wang, A. Pan, S. Liang, Observation of pseudocapacitive effect and fast ion diffusion in bimetallic sulfides as an advanced sodium-ion battery anode, Adv. Energy Mater. 8 (2018), 1703155.

[49] G. Fang, Q. Wang, J. Zhou, Y. Lei, Z. Chen, Z. Wang, A. Pan, S. Liang, Metal organic framework-templated synthesis of bimetallic selenides with rich phase boundaries for sodium-ion storage and oxygen evolution reaction, ACS Nano 13 (2019) 5635.

[50] S. Fan, S. Huang, Y. Chen, Y. Shang, Y. Wang, D. Kong, M.E. Pam, L. Shi, Y.V. Lim, Y. Shi, H.Y. Yang, Construction of complex NiS multi-shelled hollow structures with enhanced sodium storage, Energy Storage Mater (2019), https://doi.org/10.1016/j.ensm.2019.05.043.

[51] H. Yin, M. Cao, X. Yu, H. Zhao, Y. Shen, C. Li, M. Zhu, Self-standing Bi_2O_3 nanoparticles/carbon nanofiber hybrid films as a binder-free anode for flexible sodium-ion batteries, Mater. Chem. Front. 1 (2017) 1615.

[52] X. Yu, L. Wang, H. Yin, Hierarchical heterojunction structures based-on layered Sb_2Te_3 nanoplate@rGO for extended long-term life and high-rate capability of sodium batteries, Appl. Mater. Today 15 (2019) 582.

[53] S. Huang, L. Liu, Y. Zheng, Y. Wang, D. Kong, Y. Zhang, Y. Shi, L. Zhang, O. G. Schmidt, H.Y. Yang, Efficient sodium storage in rolled-up amorphous Si nanomembranes, Adv. Mater. 30 (2018), 1706637.

[54] B. Xiao, P. Wang, Z. He, Zhuo Yang, L. Tang, C. An, J. Zheng, Effect of MgO and TiO_2 coating on electrochemical performance of Li-rich cathode materials for lithium-ion batteries, Energy Technol. (2018), https://doi.org/10.1002/ente.201800829.

[55] J. Zheng, Z. Yang, A. Dai, L. Tang, H. Wei, Y. Li, Z. He, J. Lu, Boosting cell performance of $LiNi_{0.8}Co_{0.15}Al_{0.05}O_2$ via surface structure design, Small 15 (2019), 1904854.

[56] J. Zheng, Z. Yang, Z. He, H. Tong, W. Yu, J. Zhang, In situ formed $LiNi_{0.8}Co_{0.15}Al_{0.05}O_2$@$Li_4SiO_4$ composite cathode material with high rate capability and long cycling stability for lithium-ion batteries, Nano Energy 53 (2018) 613.

[57] C. An, Y. Yuan, B. Zhang, L. Tang, B. Xiao, Z. He, J. Zheng, J. Lu, Graphene wrapped $FeSe_2$ nano-microspheres with high pseudocapacitive contribution for enhanced Na-ion storage, Adv. Energy Mater. 9 (2019), 1900356.

[58] S. Huang, S. Fan, L. Xie, Q. Wu, D. Kong, Y. Wang, Y.V. Lim, M. Ding, Y. Shang, S. Chen, H.Y. Yang, Promoting highly reversible sodium storage of iron sulfide hollow polyhedrons via cobalt incorporation and graphene wrapping, Adv. Energy Mater. 9 (2019), 1901584.